

Article

# Innovative Design of Bismuth-Telluride-Based Thermoelectric Transistors

Hao Deng <sup>†</sup>, Bohang Nan <sup>†</sup> and Guiying Xu <sup>\*</sup>

School of Materials Science and Engineering, University of Science and Technology Beijing, Beijing 100083, China

<sup>\*</sup> Correspondence: [guiyingxu@126.com](mailto:guiyingxu@126.com)<sup>†</sup> These authors contributed equally to this work.

**Abstract:** Conventional thermoelectric generators, predominantly based on the  $\pi$ -type structure, are severely limited in their applications due to the relatively low conversion efficiency. In response to the challenge, in this work, a  $\text{Bi}_2\text{Te}_3$ -based thermoelectric transistor driven by laser illumination is demonstrated. Under laser illumination, a temperature difference of  $46.7\text{ }^\circ\text{C}$  is produced between the two ends of the transistor structure. Further, the hole concentrations in each region redistribute and the built-in voltages decrease due to the temperature difference, leading to the formation of the transistor circuit. Additionally, the operation condition of the thermoelectric transistor is presented. The calculation results demonstrate that the maximum output power of such a designed thermoelectric transistor is  $0.7093\text{ }\mu\text{W}$ .

**Keywords:**  $\text{Bi}_2\text{Te}_3$ ; thermoelectric transistor; output performance; theoretical calculation

## 1. Introduction

Fossil fuels, being the primary and nonrenewable energy source that has driven human society and industrial development since the Industrial Revolution, are facing an inevitable depletion due to the ever-growing demand. The resulting concerns over energy security have also contributed to escalated global conflicts [1]. Therefore, it is imperative to focus on the development of clean, low-carbon, secure, and efficient renewable energy sources.

Thermoelectric generators, capable of converting heat into electricity through the Seebeck effect, have emerged as a promising energy conversion technology [2]. Conventional thermoelectric generators typically consist of multiple thermoelectric modules, offering numerous advantages, such as high safety, extended service life, zero waste generation, no noise, and simple structure [3]. However, the applications of conventional thermoelectric generators are limited due to their relatively poor output performance. Therefore, thermoelectric generators can only be used in a few specific scenarios, such as medicine, aerospace, and military sectors.

In general, the output performance of thermoelectric generators was assessed based on the  $zT$  value of materials, output power, and conversion efficiency. To enhance the output performance, the combination of thermoelectric generators with transistor technology has been proposed [4,5]. Bejenari et al. studied the thermoelectric performance of  $\text{Bi}_2\text{Te}_3$  nanowires in the transistor structure under the gate voltage. Theoretical results indicated that the  $zT$  value could reach 3.4 for  $\text{Bi}_2\text{Te}_3$  nanowires [6]. Subsequently, Qin et al. found that the  $zT$  values of N-type and P-type  $\text{Bi}_2\text{Te}_3$  films could reach 1.22 and 1.02 in the transistor structure through experimental measurement [7]. Furthermore, Nan et al. studied the output performance of a thermoelectric transistor driven by the Seebeck effect, in which the built-in electric field is perpendicular to the gradient temperature field. Results showed that the output power was  $17.8\text{ mW}$  and conversion efficiency could reach  $8.69\%$  at a temperature difference of  $50\text{ }^\circ\text{C}$  [8,9].

These research results demonstrated that the output performance of thermoelectric generators could be significantly improved through the transistor effect. In this work, a



Citation: Deng, H.; Nan, B.; Xu, G.

Innovative Design of Bismuth-Telluride-Based Thermoelectric Transistors. *Materials* **2023**, *16*, 5536. <https://doi.org/10.3390/ma16165536>

Academic Editor: Slavko Bernik

Received: 19 June 2023

Revised: 29 July 2023

Accepted: 4 August 2023

Published: 9 August 2023



**Copyright:** © 2023 by the authors. Licensee MDPI, Basel, Switzerland. This article is an open access article distributed under the terms and conditions of the Creative Commons Attribution (CC BY) license (<https://creativecommons.org/licenses/by/4.0/>).

$\text{Bi}_2\text{Te}_3$ -based thermoelectric transistor driven by the laser illumination is presented. On the one hand, the short pulse width of a laser allows for rapid creation of a temperature difference between the two ends of the device, reaching nanosecond levels [10]. On the other hand,  $\text{Bi}_2\text{Te}_3$ -based materials exhibit excellent thermoelectric properties at room temperature [11]. Moreover, utilizing  $\text{Bi}_2\text{Te}_3$ -based materials as research subjects can improve the accuracy of theoretical calculations due to their comprehensive performance parameters [12,13]. As a result, in this work, theoretical results indicated that the maximum output power of a single  $\text{Bi}_2\text{Te}_3$ -based thermoelectric transistor could reach  $0.7093 \mu\text{W}$  with a temperature difference of  $46.7^\circ\text{C}$ . Conventional thermoelectric generators would require multiple thermoelectric modules connected in series to achieve such output performance [14–16].

## 2. Theoretical Foundations

The structure of the designed structure is depicted in the following Figure 1.

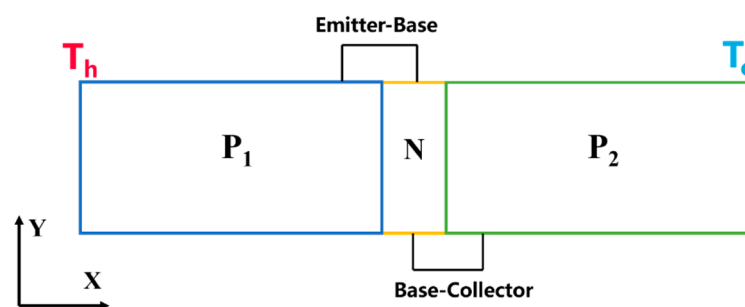


**Figure 1.** Diagram of thermoelectric transistor in X–Y plane.

Considering the one-dimensional model, the length ( $x_1$ ) of  $P_1$  region ( $P_1\text{-Bi}_2\text{Te}_3$ ) is  $1 \mu\text{m}$ , while the length of ( $x_2$ )  $P_2$  region ( $P_2\text{-Si}$ ) is  $4 \mu\text{m}$ . The scale of N region (N-Si) is the nanometer range, which can be neglected for calculation purposes.

Using a laser as the heat source, serving as the triggering condition, the  $P_1\text{-Bi}_2\text{Te}_3$  is irradiated by the laser at one end, causing its temperature to rise. Subsequently, the heat is transmitted throughout the entire structure via thermal conduction, forming a temperature field along the X direction. The temperature field induces the redistribution of majority charge carriers (holes) within the structure. The holes in  $P_1$  region and  $P_2$  region diffuse from the hot end to the cold end, accumulating at the cold end. Simultaneously, the built-in voltage across  $P_1\text{-N}$  junction decreases from the cold end to the far end. Consequently, the balance between the diffusion potential and drift potential on both sides of  $P_1\text{-N}$  junction is disrupted, leading to the injection of holes from  $P_1$  region into N-type region at the cold end. Additionally, since the length of N-type region is on the nanoscale, the holes further migrate towards  $P_2$  region. Subsequently, the accumulated holes in  $P_2$  region flow back to the N-type region along the wires. The migration of holes is consistent with the common base circuit of a bipolar transistor. Thus, it is inferred that the transistor circuit can be formed in the PNP structure under laser irradiation. In other words, the cold side of the  $P_1$  region ( $x_1$ ) functions as the emitter of the thermoelectric transistor, while the hot side of the  $P_2$  region ( $x_2$ ) serves as the collector, with the N-type region acting as the base [17].

### 2.1. Temperature Distribution of $\text{Bi}_2\text{Te}_3$ and p-Type Si under Laser Irradiation

#### 2.1.1. Calculation of Temperature Distribution in $P_1\text{-Bi}_2\text{Te}_3$

When a laser is incident upon  $\text{Bi}_2\text{Te}_3$ , according to Lambert's law, it is known that the amount of light absorbed is closely related to the position in the one-dimensional model. The closer the position is to the source of light, the greater the light absorption. Assuming material thermal capacitance is uniform, a temperature gradient will form parallel to the direction of illumination. According to Fourier's law, heat conduction will also occur along

the direction of the incident light. Taking all these considerations into account under the one-dimensional condition, the following equation can be derived [18]:

$$\rho c \frac{\partial T_1}{\partial t} = \frac{\partial}{\partial x} \left( k \frac{\partial T_1}{\partial x} \right) + (1 - R) \alpha I_0 e^{-\alpha x} \quad (1)$$

where  $\rho$  represents material density,  $c$  represents material-specific heat capacity,  $T_1$  is the temperature,  $k$  represents thermal conductivity,  $R$  represents reflectivity,  $I_0$  represents light intensity,  $t$  represents time,  $x$  is the material length along the direction of illumination, and  $\alpha$  represents absorption coefficient.

Due to the extremely short duration of the pulse laser, it can be assumed that there is no heat transfer occurring at the ends of the sample. Therefore, the following conditions hold:

$$\frac{\partial T_1(x=0, t)}{\partial x} = 0 \quad (2)$$

$$\frac{\partial T_1(x=l, t)}{\partial x} = 0 \quad (3)$$

In addition, the initial temperature distribution of the sample is assumed to be uniform, with no heat transfer occurring between different parts of the sample. In other words, the temperature at each position is a constant, given by:

$$T_1(x, 0) = \varphi_1(x) = \text{constant} \quad (4)$$

By solving these equations in MATLAB R2020a, the temperature distribution  $T_1(x_1)$  in  $P_1\text{-Bi}_2\text{Te}_3$  can be obtained.

### 2.1.2. Calculation of Temperature Distribution in $P_2\text{-Si}$

Unlike the calculation of temperature distribution in  $\text{Bi}_2\text{Te}_3$ , the differential equation for the temperature distribution in  $P_2\text{-Si}$  does not include the influence of illumination; thus, it becomes a one-dimensional heat conduction problem without a heat source:

$$\rho c \frac{\partial T_2}{\partial t} = \frac{\partial}{\partial x} \left( k \frac{\partial T_2}{\partial x} \right) \quad (5)$$

Similarly, the boundary conditions can be set as follows:

$$\frac{\partial T_2(x=0, t)}{\partial x} = 0 \quad (6)$$

$$\frac{\partial T_2(x=l, t)}{\partial x} = 0 \quad (7)$$

The initial condition for the  $P_2\text{-Si}$  sample is:

$$T_2(x, 0) = \varphi_2(x) = \text{constant} \quad (8)$$

By solving these equations in MATLAB R2020a, the temperature distribution  $T_2(x_2)$  in  $P_2\text{-Si}$  can be obtained.

## 2.2. Hole Concentration Distribution in $\text{Bi}_2\text{Te}_3$ and $P_2\text{-Si}$

### 2.2.1. Hole Concentration Distribution in $P_1\text{-Bi}_2\text{Te}_3$

When  $P_1\text{-Bi}_2\text{Te}_3$  is subjected to a stable temperature field at 20 °C, the hole concentration is uniformly distributed, which is equal to the acceptor concentration  $P_a$ . Subsequently, when  $P_1\text{-Bi}_2\text{Te}_3$  is influenced by a temperature gradient ( $dx/dt \neq 0$ ), the holes redistribute, while the acceptor ions remain fixed. The redistribution of holes can be obtained through theoretical analysis, as shown below.

DC transport equation for current [19]:

$$J_p(x) = \sigma_p(x)[E(x) - S_p(x)\nabla T(x)] \quad (9)$$

$$E(x) = \frac{d\varphi(x)}{dx} \quad (10)$$

where  $J_p(x)$  represents the current density,  $\nabla T(x)$  is the temperature gradient,  $E(x)$  denotes the electric field,  $\varphi(x)$  represents the electric potential,  $\sigma_p(x)$  is the electrical conductivity of P<sub>1</sub>-Bi<sub>2</sub>Te<sub>3</sub>, and  $S_p(x)$  is the Seebeck coefficient p-type Bi<sub>2</sub>Te<sub>3</sub>.

One-dimensional Poisson equation [20]:

$$\frac{d^2\varphi(x)}{dx^2} = -\frac{e}{\epsilon_r\epsilon_0}[p_1(x_1) - P_a] \quad (11)$$

where  $e$  is the electronic charge,  $\epsilon_r$  is the relative permittivity,  $\epsilon_0$  is the vacuum permittivity,  $p_1(x_1)$  represents the hole concentration distribution in P<sub>1</sub>-Bi<sub>2</sub>Te<sub>3</sub>, and  $P_a$  is the constant concentration of acceptor holes assuming complete ionization of Bi<sub>2</sub>Te<sub>3</sub>.

Continuity equation [21]:

$$\frac{\partial p_1(x_1)}{\partial t} = -\frac{1}{q}\frac{\partial J_p(x)}{\partial x} + (G_p - R_p) \quad (12)$$

where  $G_p$  is the hole carrier generation rate in Bi<sub>2</sub>Te<sub>3</sub>, and  $R_p$  is the hole carrier recombination rate.

Since P<sub>1</sub>-Bi<sub>2</sub>Te<sub>3</sub> discussed in this work is a degenerate semiconductor,  $\sigma_p(x)$  and  $S_p(x)$  can be expressed as [11,22]:

$$\sigma_p(x) = p(x)e\mu_p \quad (13)$$

$$S_p(x) = \left[ \frac{8\pi^{\frac{8}{3}}m_p^*k_B^2(r + \frac{3}{2})}{3^{\frac{5}{3}}h^2e} \right] \frac{T_1(x_1)}{p_1(x_1)^{\frac{2}{3}}} \quad (14)$$

where  $\mu_p$  represents the hole mobility of P<sub>1</sub>-Bi<sub>2</sub>Te<sub>3</sub>,  $r$  is the scattering factor ( $= -1/2$ ),  $h$  is the Planck constant,  $m_p^*$  denotes the effective mass, and  $T_1(x_1)$  is temperature distribution of P<sub>1</sub>-Bi<sub>2</sub>Te<sub>3</sub> along the  $x$  direction.

Since the simulated temperature distribution is significantly lower than the intrinsic excitation temperature of Bi<sub>2</sub>Te<sub>3</sub>, it can be assumed that  $G_p = R_p$  and the total hole concentration in Bi<sub>2</sub>Te<sub>3</sub> remains constant after applying the temperature gradient:

$$\int_0^{l_x} P_a dx = \int_0^{l_x} p_1(x_1) dx \quad (15)$$

Substituting the above equation into Equation (10) can obtain:

$$E(x) = \frac{d\varphi(x)}{dx} = \int_0^{l_x} \frac{-e}{\epsilon_r\epsilon_0}[p_1(x_1) - P_a] dx = 0 \quad (16)$$

Substituting Equation (16) into Equation (9) yields:

$$J_p(x) = -\sigma_p(x)S_p(x)\nabla T(x) \quad (17)$$

Furthermore, assuming that the entire P<sub>1</sub>-Bi<sub>2</sub>Te<sub>3</sub> reaches a stable state after the temperature distribution is established, Equation (12) can be written as:

$$\frac{\partial p}{\partial t} = -\frac{1}{q}\frac{\partial J_p(x)}{\partial x} = 0 \quad (18)$$

By solving these equations in MATLAB, the hole concentration distribution of P<sub>1</sub>-Bi<sub>2</sub>Te<sub>3</sub> can be obtained under a temperature gradient.

### 2.2.2. Hole Concentration Distribution in P<sub>2</sub>-Si

Since the carrier concentration of P<sub>2</sub>-Si studied in this work is less than 10<sup>18</sup> cm<sup>-3</sup>, it is considered a nondegenerate semiconductor. Therefore, the Seebeck coefficient can be expressed as [23]:

$$S_p(x) = \frac{k_B}{e} \left[ \left( r + \frac{5}{2} \right) + \ln \frac{2(2\pi m^* k_B T_2(x_2))^{3/2}}{h^3 n} \right] \quad (19)$$

Then, based on the temperature distribution  $T_2(x_2)$  in P<sub>2</sub>-Si and Equations (13), (15), (17), and (18), the hole concentration distribution of P<sub>2</sub>-Si can be derived.

### 2.3. Operation Conditions of Thermoelectric Transistor

In order for the thermoelectric transistor to operate properly, it must be in a forward-active mode [17]. Since the formation for the circuit of the thermoelectric transistor is only based on the Seebeck effect, the potential within it can be represented by the concentration distribution in each region. Therefore, it is crucial to determine appropriate concentration ranges within each region to ensure the normal operation of the thermoelectric transistor.

Firstly, the thermoelectric transistor is composed of P<sub>1</sub>-Bi<sub>2</sub>Te<sub>3</sub>, N-Si, and P<sub>2</sub>-Si materials. Before applying a temperature gradient (the entire transistor is at  $T = 20$  °C), the respective donor or acceptor doping ion concentrations must be greater than their intrinsic carrier concentrations. Mathematically, it can be expressed as follows:

$$P_{a1} > p_{i1}(T = 20 \text{ °C}) \quad (20)$$

$$N_d > n_i(T = 20 \text{ °C}) \quad (21)$$

$$P_{a2} > p_{i2}(T = 20 \text{ °C}) \quad (22)$$

where  $P_{a1}$ ,  $N_d$ , and  $P_{a2}$  represent the doping concentrations in P<sub>1</sub> region (P<sub>1</sub>-Bi<sub>2</sub>Te<sub>3</sub>, emitter), N region (N-Si, base), and P<sub>2</sub> region (P<sub>2</sub>-Si, collector), respectively.  $p_{i1}$ ,  $n_i$ , and  $p_{i2}$  represent the intrinsic carrier concentrations in the respective regions at  $T = 20$  °C.

#### 2.3.1. Implementation of Forward Bias and Forward Conduction at the Emitter–Base

After applying a temperature gradient, the emitter (P<sub>1</sub> region) and the base (N region) should simultaneously satisfy the forward bias and forward conduction. The temperature distribution  $T_1(x_1)$  between P<sub>1</sub> region and N region can be obtained from the previous section. According to the relevant literature [24], the built-in voltage at the emitter–base junction varies with temperature:

$$V_{bi1}(x_1) = \frac{k_B T_1(x_1)}{q} \left[ \ln \frac{P_{a1}}{p_{i1}(x_1)} + \ln \frac{N_d}{n_i(x_1)} \right] \quad (23)$$

where  $k_B$  is the Boltzmann constant,  $p_{i1}(x_1)$  is the intrinsic carrier concentration affected by the temperature distribution  $T_1(x_1)$ , while  $P_{a1}$  and  $N_d$  remain constant regardless of the applied temperature gradient. The variations in  $p_{i1}(x_1)$  and  $n_i(x_1)$  with the temperature distribution can be described by the following [25,26]:

$$p_{i1}(x_1) = \left( \frac{m_{p1}^*}{m_e} \right)^{\frac{3}{2}} \times \left( \frac{T_1(x_1)}{300} \right)^{\frac{3}{2}} \times \exp \left( -\frac{E_{gp1}}{T_1(x_1)} \right) \times 2.5 \times 10^{19} \quad (24)$$

$$n_i(x_1) = 5.23 \times 10^{15} \times T_1(x_1)^{\frac{3}{2}} \times \exp \left( \frac{6395.39}{T_1(x_1)} \right) \quad (25)$$

where  $m_{p1}^*$  is the effective mass of the emitter,  $m_e$  is the electron mass, and  $E_{gp1}$  is the bandgap of the emitter.

To achieve forward bias and forward conduction at the emitter–base junction, the built-in voltage  $V_{bi1}(x_1)$  should satisfy:

$$V_{bi1}(x_1) > 0 \quad (26)$$

Additionally, after applying the temperature gradient, the potential of the emitter should be higher than that of the base:

$$\varphi_{p1}(x_1) > \varphi_n(x_1) \quad (27)$$

Since the potential of each region in this work is mainly determined by its carrier concentration, Equation (27) can be written as:

$$p_1(x_1) > N_d \quad (28)$$

where  $p_1(x_1)$  is the hole concentration distribution of the emitter after applying the temperature gradient. However, the concentration of the base remains constant ( $N_d$ ) because it is completely depleted.

Finally, in order to ensure the forward conduction in the thermoelectric transistor, the generated voltage due to the Seebeck effect (the Seebeck voltage  $V_{s1}(x_1)$ ) should be greater than the built-in voltage  $V_{bi1}(x_1)$ . In other words, the emitter voltage  $V_e(x_1)$  should be greater than 0:

$$V_e(x_1) = V_{s1}(x_1) - V_{bi1}(x_1) > 0 \quad (29)$$

$$V_{s1}(x_1) = \Delta T(x_1) \times S_1 \quad (30)$$

$$S_1 = \left[ \frac{8\pi^{\frac{8}{3}} m_{p1}^* k_B^2 (r + \frac{3}{2})}{3^{\frac{5}{3}} h^2 e} \right] \left[ \frac{T_1(x_1)}{p_1(x_1)^{\frac{2}{3}}} \right] \quad (31)$$

where  $S_1$  represents the Seebeck coefficient of the emitter and  $\Delta T(x_1)$  is the temperature distribution between the emitter and the base. By combining these equations, the forward bias and forward conduction at the emitter–base can be achieved.

### 2.3.2. Realization of Reverse Bias at the Base–Collector

Similarly, the intrinsic carrier concentration distribution of P<sub>2</sub>-type region (P<sub>2</sub>-Si) under the applied temperature gradient can be expressed [25]:

$$p_{i2}(x_2) = 5.23 \times 10^{15} \times T_2(x_2)^{\frac{3}{2}} \times \exp\left(\frac{6395.39}{T_2(x_2)}\right) \quad (32)$$

In order to ensure the normal operation of the thermoelectric transistor, the base–collector junction should be the reverse bias. Under the influence of the temperature distribution  $T_2(x_2)$ , the built-in voltage at the base–collector junction can be expressed as:

$$V_{bi2}(x_2) = \frac{k_B T(x_2)}{q} \left[ \ln \frac{P_{a2}}{p_{i2}(x_2)} + \ln \frac{N_d}{n_i(x_2)} \right] \quad (33)$$

To ensure proper operation,  $V_{bi2}(x_2)$  must be positive:

$$V_{bi2}(x_2) > 0 \quad (34)$$

Similar to the emitter–base junction, the potential of the base should be higher than that of the collector:

$$\varphi_n(x_2) > \varphi_{p2}(x_2) \tag{35}$$

$$N_d > p_2(x_2) \tag{36}$$

Furthermore, the Seebeck coefficient and the Seebeck voltage for P<sub>2</sub>-Si are expressed as follows:

$$V_{s2}(x_2) = \Delta T(x_2) \times S_2 \tag{37}$$

$$S_2 = \frac{k_B}{e} \left[ \left( r + \frac{5}{2} \right) + \ln \frac{2 \left( 2\pi m_{p2}^* k_B T_2(x_2) \right)^{3/2}}{h^3 p_2(x_2)} \right] \tag{38}$$

where  $p_2(x_2)$  is the hole concentration distribution in the collector region after applying the temperature gradient.

By solving these equations, the operation conditions of the base–collector junction can be determined.

#### 2.4. The Output Performance of Thermoelectric Transistors

For bipolar thermoelectric transistors, the base–collector circuit can be considered as the output circuit. In this work, the early voltage effects of the emitter, base, and collector, as well as the contact resistance between the transistor and the electrodes, can be neglected. The corresponding equivalent DC circuit diagram is shown in Figure 2. The left side of the circuit diagram represents the equivalent circuit of the emitter–base junction.  $V_{s1}(x_1)$  denotes the Seebeck voltage generated in the P<sub>1</sub> region, serving as the external voltage at the emitter.  $R_e(x_1)$  represents the resistance of the P<sub>1</sub> region of the emitter.  $V_{bi1}(x_1)$  is assumed to be the forward voltage. On the right side of the circuit, the equivalent circuit of the base–collector junction is shown.  $V_{s2}(x_2)$  signifies the Seebeck voltage generated in the P<sub>2</sub> region, acting as the external voltage at the collector.  $R_c(x_2)$  corresponds to the resistance of the P<sub>2</sub> region of the collector.  $V_{bi2}(x_2)$  is the voltage influenced by the emitter current  $I_e(x_1)$ . Furthermore, considering that the thickness of the base can be neglected compared to the emitter and collector and that it is fully depleted, the collector current  $I_c(x_2)$  can be assumed to be equal to the emitter current  $I_e(x_1)$ .

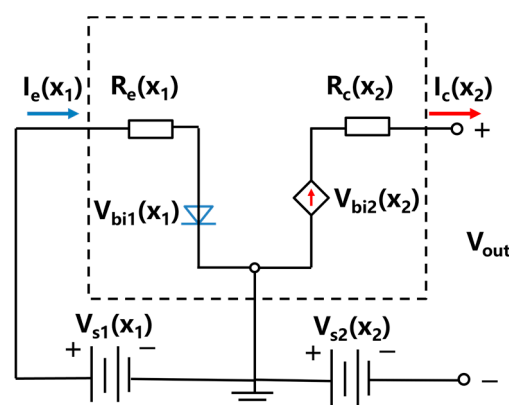


Figure 2. Schematic diagram of equivalent circuit in thermoelectric transistor.

According to the Kirchhoff’s law, the relationships among these electrical parameters can be expressed:

$$V_e(x_1) = V_{s1}(x_1) - V_{bi1}(x_1) = I_e(x_1)R_e(x_1) \tag{39}$$

$$V_c(x_2) = V_{bi2}(x_2) - V_{s2}(x_2) = I_c(x_2)R_c(x_2) \tag{40}$$

$$I_e(x_1) = I_c(x_2) \tag{41}$$

$$R_e(x_1) = \frac{1}{p_{a1}e\mu_{p1}} \times \frac{l_{x1}}{w_y h_z} \quad (42)$$

$$R_c(x_2) = \frac{1}{p_{a2}e\mu_{p2}} \times \frac{l_{x2}}{w_y h_z} \quad (43)$$

where  $V_e(x_1)$  is the emitter voltage,  $V_c(x_2)$  is the collector voltage, and  $\mu_{p1}$  and  $\mu_{p2}$  are the hole mobility of the P<sub>1</sub>-type material (P<sub>1</sub>-Bi<sub>2</sub>Te<sub>3</sub>) and P<sub>2</sub>-type material (P<sub>2</sub>-Si), respectively.  $l_{x1}$  and  $l_{x2}$  represent the lengths of the P<sub>1</sub>-type and P<sub>2</sub>-type materials along the  $x$  direction, while  $w_y$  and  $h_z$  denote the lengths of the device in  $y$  and  $z$  directions, respectively, with values set to 1  $\mu\text{m}$ .  $S_{p2}$  is the Seebeck coefficient of the collector and  $m_{p2}^*$  is the effective mass of the collector.

The output power of the transistor can be expressed as the product of the open-circuit voltage and the short-circuit current:

$$P_{out} = I_e(x_1) \times V_{out} = I_e(x_1) \times V_c(x_2) = I_e(x_1) \times [V_{bi2}(x_2) - V_{s2}(x_2)] \quad (44)$$

### 2.5. The Material Parameters of Thermoelectric Transistor

In this work, P<sub>1</sub>-Bi<sub>2</sub>Te<sub>3</sub>, N-Si, and P<sub>2</sub>-Si are selected as the emitter material, base material, and collector material, respectively. The material parameters of the thermoelectric transistor studied are listed in Table 1.

**Table 1.** Material parameters of thermoelectric transistor.

Parameter	Emitter	Base	Collector	Ref.
$E_g$ (eV)	0.18	1.12	1.12	[25,27]
$m^*/m_e$	1.4671	0.43	0.2601	[28–30]
$\epsilon_r$	90	11.7	11.7	[6,25]
$\mu_p$ (cm <sup>2</sup> /V s)	510	-	480	[21,25]

## 3. Results and Discussion

### 3.1. Temperature Distribution in Thermoelectric Transistor

#### 3.1.1. Temperature Distribution in p-Type Bi<sub>2</sub>Te<sub>3</sub>

It is assumed that P<sub>1</sub>-Bi<sub>2</sub>Te<sub>3</sub> is in the temperature of 20 °C. Under the condition of illuminating with an incident optical power of  $=3 \times 10^7$  (W·cm<sup>-2</sup>) for a duration of 100 ns, the temperature distribution within Bi<sub>2</sub>Te<sub>3</sub> is obtained as shown in Figure 3.

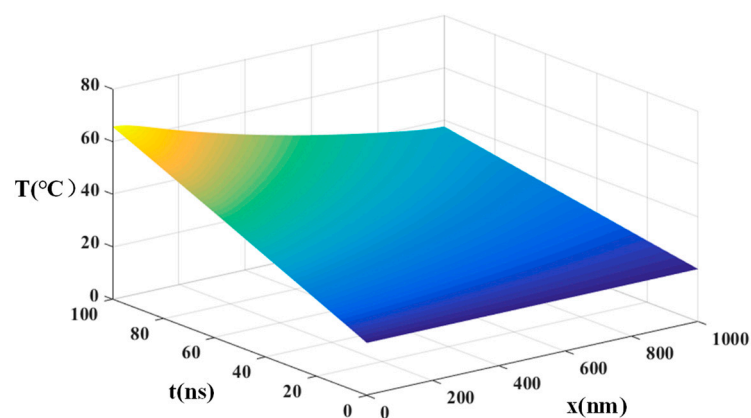


**Figure 3.** Temperature distribution of Bi<sub>2</sub>Te<sub>3</sub> after laser irradiation with time  $t$  and  $x$ .

As depicted in Figure 3, it is apparent that, with an increase in laser irradiation time, the sample initiates heating from the irradiated surface at  $x = 0 \mu\text{m}$ . Subsequently, the heat gradually propagates throughout the entire device, and the lowest temperature is

observed at  $x = 1 \mu\text{m}$  within  $P_1$  region. Figure 4 illustrates the temperature distribution in  $P_1$  region at  $T = 100 \text{ ns}$ . Notably, after 100 ns of illumination, the temperature distribution in  $P_1$  region ( $\text{Bi}_2\text{Te}_3$ ) exhibits a pattern of decreasing temperature as the distance from the laser increases. Specifically, at  $x = 0 \mu\text{m}$ , the temperature at 100 ns is  $T_{b1} = 66.7 \text{ }^\circ\text{C}$ , whereas, at  $x = 1 \mu\text{m}$ , the temperature reaches its minimum value of  $T_{b2} = 37 \text{ }^\circ\text{C}$ . By employing a quadratic function, the temperature variation  $T_1(x_1)$  in  $P_1$  region as a function of  $x$  can be obtained:

$$T_1(x_1) = 14.35x_1^2 - 43.95x_1 + 66.7 \quad (45)$$

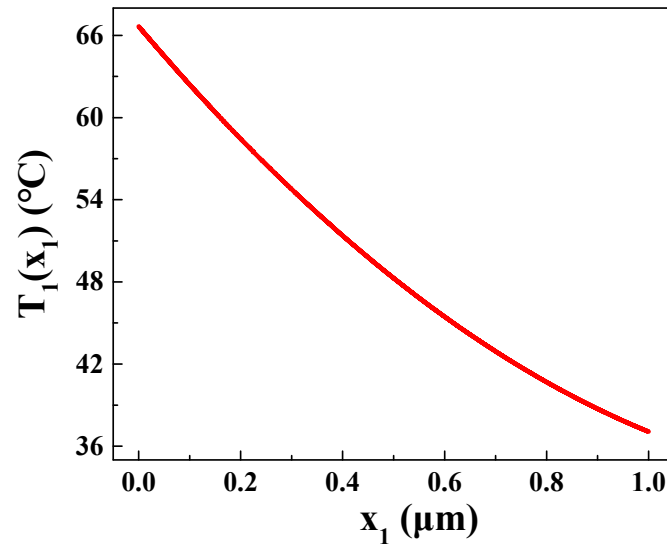


Figure 4. Temperature distribution in  $P_1$  region at  $t = 100 \text{ ns}$ .

### 3.1.2. Temperature Distribution in p-Si

By solving the equations in MATLAB, the temperature distribution in  $P_2$  region ( $P_2\text{-Si}$ ) along the  $x$  direction can be obtained. After 100 ns, the temperature distribution is shown in Figure 5.

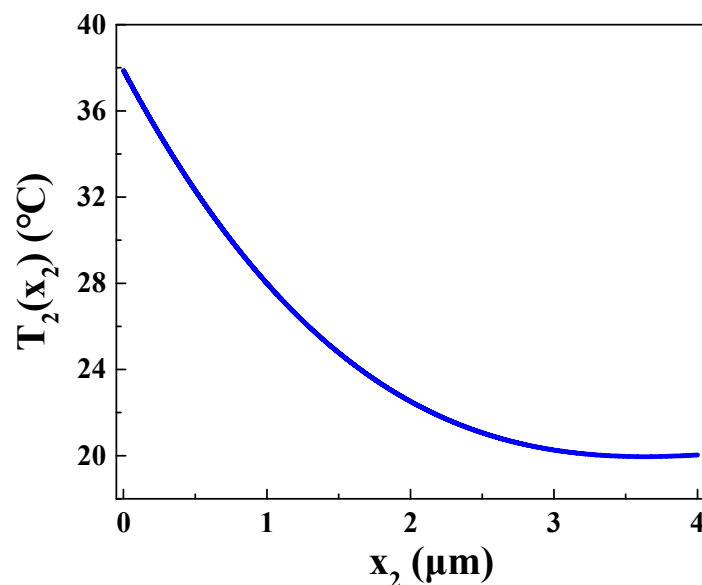


Figure 5. Temperature distribution in  $P_2$  region at  $t = 100 \text{ ns}$ .

Based on Figure 5, it can be observed that the temperature distribution in  $P_2$ -type region gradually decreases with increasing  $x$ . It is important to note that n-type region in

this work is extremely thin. Therefore, the length of the n-type region along the  $x$  direction is assumed to be 0, implying that  $x_1 = 1 \mu\text{m}$  coincides with  $x_2 = 0 \mu\text{m}$ . At  $x_2 = 0 \mu\text{m}$ , P<sub>2</sub>-Si exhibits the highest temperature,  $T_{s1} = 37^\circ\text{C}$ , while, at  $x_2 = 4 \mu\text{m}$ , p-Si reaches its lowest temperature,  $T_{s2} = 20^\circ\text{C}$ . By fitting a curve to the data in the figure, a fitting function  $T_2(x_2)$  for the temperature distribution in P<sub>2</sub>-Si can be obtained:

$$T_2(x_2) = -0.1982x_2^3 + 2.798x_2^2 - 12.48x_2 + 37 \tag{46}$$

### 3.2. Hole Concentration Distribution within Thermoelectric Transistor

The thermoelectric transistor consists of P<sub>1</sub>-type region, N-type region, and P<sub>2</sub>-type region. As mentioned in the previous section, the temperature distribution along the  $x$  direction of the transistor is represented by Equations (45) and (46).

Considering that N-type region is assumed to be completely depleted, it contains no free mobile carriers. However, for both P<sub>1</sub>-type region and P<sub>2</sub>-type region, under the influence of temperature distribution, the holes migrate from the hot end to the cold end, leading to their accumulation at the cold end. By utilizing the calculation formula from the previous section, the concentration distribution of holes in P<sub>1</sub>-type region can be obtained:

$$p_1(x_1) = \frac{P_{a1} \times (-6.429 \times 10^{-13})}{(x_1 - 1.532 \times 10^{-4})^3} \tag{47}$$

From Figure 6, it is evident that  $p_1(x_1)$  increases with increasing  $x_1$ . This indicates that the hole concentration in P<sub>1</sub>-type region gradually increases from the hot end to the cold end. Additionally, as  $P_{a1}$  increases,  $p_1(x_1)$  also increases. Of note,  $p_1(x_1) = P_{a1}$  is near the midpoint of the P<sub>1</sub>-type region ( $x_{10} = 0.501 \mu\text{m}$ ), as shown in the dashed line in Figure 6. This is because the hole carriers in the P<sub>1</sub>-type region (Bi<sub>2</sub>Te<sub>3</sub>) redistribute only along the  $x$  direction, and the temperature difference is fixed. Therefore, the position  $x_{10}$  remains constant. As a result, it can be inferred that, for  $x_1 < x_{10}$ ,  $p_1(x_1) < P_{a1}$ , and, for  $x_{10} \leq x_1 \leq 1 \mu\text{m}$ ,  $p_1(x_1) \geq P_{a1}$ , with equality only at  $x_1 = x_{10}$ .

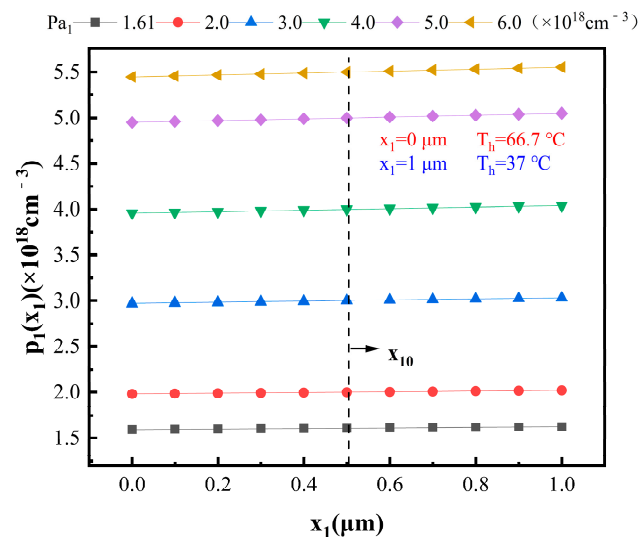


Figure 6. Relationship between  $p_1(x_1)$  and  $x_1$  at different hole concentrations.

Similarly, hole concentration distribution of P<sub>2</sub>-Si can be obtained:

$$p_2(x_2) = \frac{P_{a2} \times (5.773 \times 10^4)}{(1.858 \times 10^8 \times x_2^2 - 1.749 \times 10^5 \times x_2 + 39)^3} \tag{48}$$

Figure 7 illustrates the variation in  $p_2(x_2)$  with respect to  $x_2$  for different  $P_{a2}$ . It can be observed that  $p_2(x_2)$  also increases with the increase in  $x_2$ . Additionally, as  $P_{a2}$

increases,  $p_2(x_2)$  increases. Similarly, at  $x_{20} = 2.009 \mu\text{m}$ ,  $p_2(x_2)$  equals  $P_{a2}$ , as indicated by the dashed line in Figure 7. In other words, for  $0 \leq x_2 < x_{20} = 2.009 \mu\text{m}$ ,  $P_{a2} > p_2(x_2)$ , and, for  $x_{20} \leq x_2 \leq 4 \mu\text{m}$ ,  $p_2(x_2) \geq P_{a2}$ , with equality only at  $x_2 = x_{20}$ .

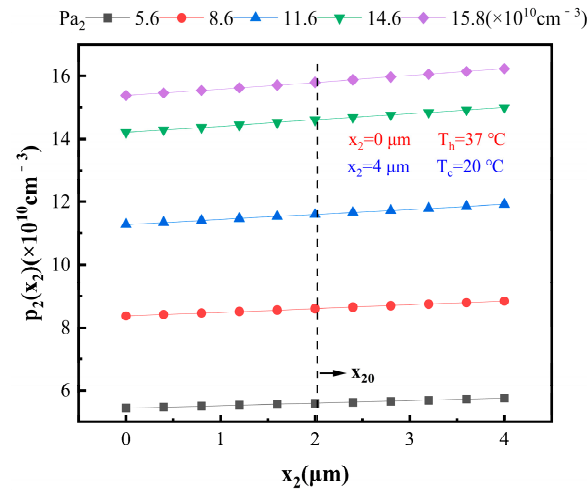


Figure 7. Relationship between  $p_2(x_2)$  and  $x_2$  at different hole concentrations.

Thus, it can be inferred that the Seebeck effect causes the redistribution of hole concentrations in both  $P_1$ -type and  $P_2$ -type regions, with holes diffusing from the hot end to the cold end. Consequently, the built-in voltage at both the  $P_1$ -N junction and the N- $P_2$  junction decreases from the cold end to the hot end. This unique characteristic enables such PNP heterojunctions to function as thermoelectric transistors. The emitter corresponds to the region with  $x_{10} \leq x_1 \leq 1 \mu\text{m}$  in the  $P_1$ -type region, the base corresponds to the entire N-type region, and the collector corresponds to the region with  $0 \leq x_2 < x_{20} = 2.009 \mu\text{m}$  in the  $P_2$ -type region.

### 3.3. Operation Conditions in Thermoelectric Transistor

#### 3.3.1. Forward Bias of Emitter–Base Junction

When the entire thermoelectric transistor is at  $20 \text{ }^\circ\text{C}$ , based on Equations (20)–(22), the required values for  $P_{a1}$ ,  $N_d$ , and  $P_{a2}$  can be determined:

$$P_{a1} > p_{i1} = 1.609 \times 10^{18} \left( \text{cm}^{-3}, T = 20 \text{ }^\circ\text{C} \right) \tag{49}$$

$$N_d > n_i = 3.179 \times 10^{10} \left( \text{cm}^{-3}, T = 20 \text{ }^\circ\text{C} \right) \tag{50}$$

$$P_{a2} > p_{i2} = 9.268 \times 10^9 \left( \text{cm}^{-3}, T = 20 \text{ }^\circ\text{C} \right) \tag{51}$$

For simplicity, their values are assumed to be  $1.61 \times 10^{18} \text{ cm}^{-3}$ ,  $3.2 \times 10^{10} \text{ cm}^{-3}$ , and  $1.0 \times 10^{10} \text{ cm}^{-3}$ , respectively.

The temperature distribution  $T_1(x_1)$  and the temperature difference  $\Delta T_1(x_1)$  for the emitter–base junction can be written:

$$T_1(x_1) = 14.35x_1^2 - 43.95x_1 + 66.7 \tag{52}$$

$$\Delta T_1(x_1) = -14.35x_1^2 - 43.95x_1 \tag{53}$$

$$x_1 \in [0.501, 1] \text{ (}\mu\text{m)} \tag{54}$$

Under this temperature distribution, the calculated values for the Seebeck coefficient  $S_1$  and the Seebeck voltage  $V_{s1}$  in  $P_1$  region are shown in Figure 8.

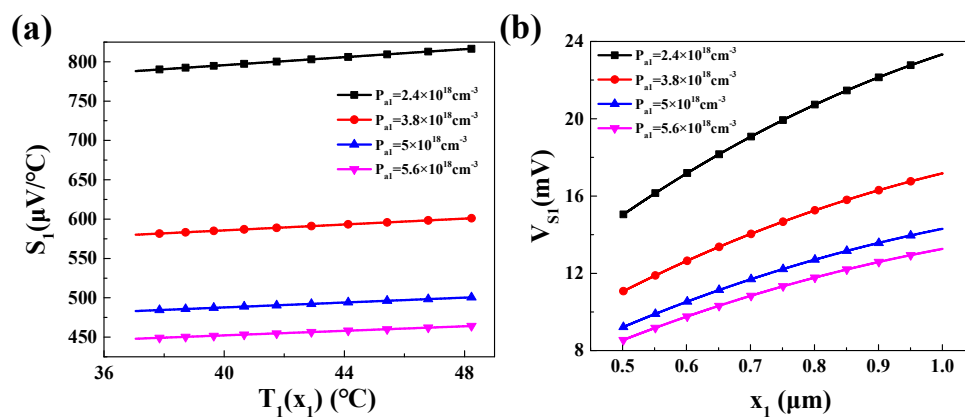


Figure 8. In the  $P_1$  region, under different doping concentrations  $P_{a1}$ : (a) the relationship between Seebeck coefficient  $S_1$  and temperature; (b) variation in Seebeck voltage  $V_{s1}$  at different  $x_1$  positions.

As shown in Figure 8, the Seebeck coefficient  $S_1$  of  $P_1$  region increases with the temperature  $T_1(x_1)$ . Moreover, for different doping concentrations  $P_{a1}$ , the smaller doping concentration leads to a larger Seebeck coefficient. As for the Seebeck voltage  $V_{s1}$ , it exhibits a trend where it increases as the distance from the hot end ( $x_1 = 0$ ) increases due to the larger temperature difference.

Additionally, the built-in voltage  $V_{bi1}$  within  $P_1$ -N region can be obtained, as shown in Figure 9.

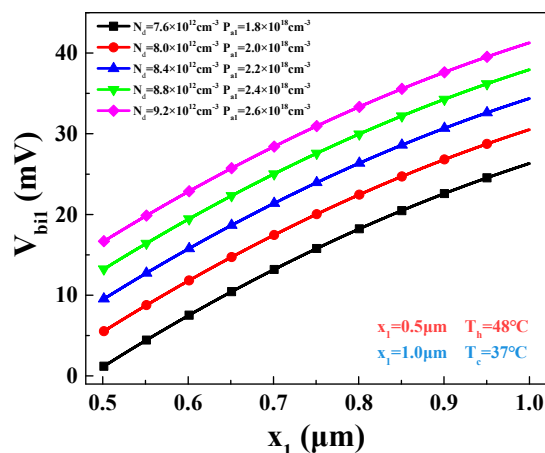


Figure 9. Different values of built-in voltage in  $P_1$ -N region on different  $x_1$ .

Under different values of  $P_{a1}$  and  $N_d$ , the built-in voltage increases with the increase in  $x_1$ . This means that, as the temperature decreases, the built-in voltage increases. The increase is primarily attributed to the decrease in intrinsic carrier concentration with decreasing temperature.

Based on Section 2.3.1, it can be concluded that achieving the forward bias and forward conduction of the emitter–base junction depends on three conditions:  $V_{bi1}(x_1) > 0$ ,  $V_e(x_1) = V_{s1}(x_1) - V_{bi1}(x_1) > 0$ , and  $p_1(x_1) > N_d$ . These conditions are all influenced by  $P_{a1}$ ,  $x_1$ , and  $N_d$ . The appropriate concentration ranges for  $P_{a1}$  and  $N_d$  are shown in Figure 10.

It can be observed that the suitable range for  $N_d$  is  $3.2 \times 10^{10} \text{ cm}^{-3} \sim 15.8 \times 10^{10} \text{ cm}^{-3}$ . As the range of  $N_d$  increases, the range of  $P_{a1}$  decreases. When  $N_d$  is  $3.2 \times 10^{10} \text{ cm}^{-3}$ , the range of  $P_{a1}$  is  $1.61 \times 10^{18} \text{ cm}^{-3} \sim 5.6 \times 10^{18} \text{ cm}^{-3}$ , as indicated by the black line. When  $N_d$  increases to  $15.8 \times 10^{10} \text{ cm}^{-3}$ , the range of  $P_{a1}$  is only  $1.61 \times 10^{18} \text{ cm}^{-3} \sim 2.0 \times 10^{18} \text{ cm}^{-3}$ , as shown by the red line. This is because the built-in voltage  $V_{bi1}(x_1)$  is positively correlated with  $N_d$  and  $P_{a1}$ . As  $N_d$  and  $P_{a1}$  increase,  $V_{bi1}(x_1)$  also increases, resulting in a smaller range of  $P_{a1}$  for achieving  $V_{s1}(x_1) - V_{bi1}(x_1) > 0$ .

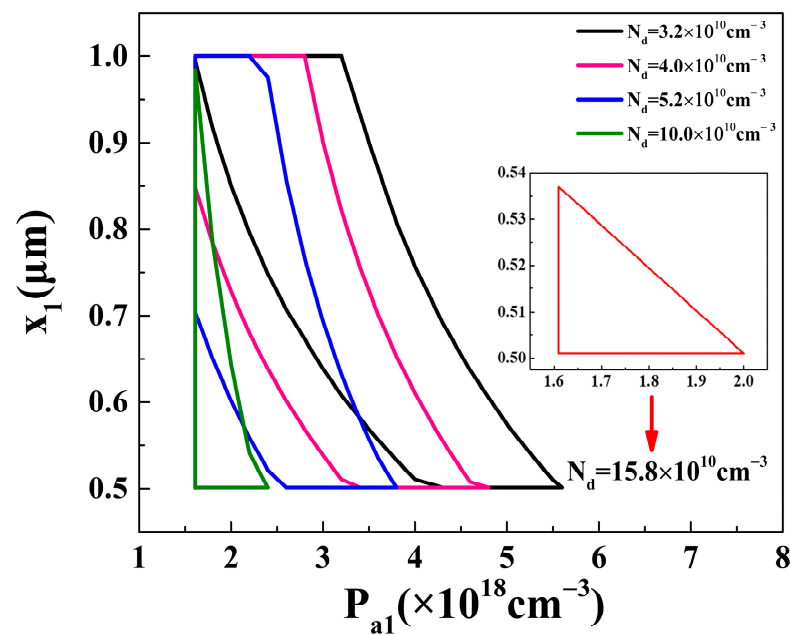


Figure 10. Suitable range and corresponding  $x_1$  value of  $P_{a1}$  that satisfies forward bias and forward conduction of emitter–base.

Additionally, it can be found that  $x_1$  also changes with  $N_d$  and  $P_{a1}$ . As  $N_d$  and  $P_{a1}$  increase, the range of  $x_1$  gradually approaches 0.501  $\mu\text{m}$ . This is because, at  $x_1 = 1 \mu\text{m}$ , both  $V_{bi1}(x_1)$  and  $V_{s1}(x_1)$  reach their maximum values. However, in comparison to  $V_{s1}(x_1)$ ,  $V_{bi1}(x_1)$  increases at a faster rate as  $x_1$  increases. Therefore, it is relatively easier to achieve the operation conditions of the emitter–base junction at  $x_1 = 0.501 \mu\text{m}$ . Thus, when  $N_d = 3.2 \times 10^{10} \text{ cm}^{-3}$ , the maximum range of  $x_1$  is 0.608  $\mu\text{m}$  to 1  $\mu\text{m}$ . While  $N_d = 15.8 \times 10^{10} \text{ cm}^{-3}$ , the maximum range of  $x_1$  is 0.501  $\mu\text{m}$  to 0.537  $\mu\text{m}$ . Therefore, the forward bias and forward conduction of the emitter–base junction can be achieved by adjusting the concentrations of  $P_{a1}$  and  $N_d$ . Such a deigned doping concentration for  $\text{P}_1\text{-Bi}_2\text{Te}_3$  can be obtained directly by doping process, e.g., phosphorus as acceptor.

### 3.3.2. Reverse Bias of Base–Collector Junction

When a temperature gradient is applied in the base–collector junction, the temperature distribution equation  $T_2(x_2)$  and temperature difference  $\Delta T_2(x_2)$  can be expressed as follows:

$$T_2(x_2) = -0.1982x_2^3 + 2.798x_2^2 - 12.48x_2 + 37 \tag{55}$$

$$\Delta T_2(x_2) = 0.1982x_2^3 - 2.798x_2^2 + 12.48x_2 - 17 \tag{56}$$

$$x_2 \in [0, 0.2] (\mu\text{m}) \tag{57}$$

It should be noted that  $\Delta T(x_1)$  represents the temperature difference between the emitter and base, with a positive value. However,  $\Delta T_2(x_2)$  represents the temperature difference between the collector and base, with a negative value. Therefore,  $V_{s1}(x_1)$  has a positive value, while  $V_{s2}(x_2)$  has a negative value.

For  $P_2$  region, the values of the Seebeck coefficient  $S_2$  and the Seebeck voltage  $V_{s2}$  are shown in Figure 11.

It can be observed that the Seebeck coefficient  $S_2$  of  $P_2$  region increases with temperature  $T_2(x_2)$ . For different doping concentrations  $P_{a2}$ , a smaller doping concentration leads to a larger Seebeck coefficient. Regarding the Seebeck voltage  $V_{s2}$ , it exhibits a trend as the position approaches  $x_2 = 0$  (closer to the hot end) due to the increasing temperature difference.

The built-in voltage  $V_{bi2}$  in the N-P<sub>2</sub> region is depicted in Figure 12. It can be found that the built-in voltage  $V_{bi2}$  increases with increasing  $x_2$  at different values of  $P_{a2}$  and  $N_d$ . In other words, as the temperature decreases, the built-in voltage increases. This increase primarily stems from the decrease in intrinsic charge carriers with decreasing temperature.

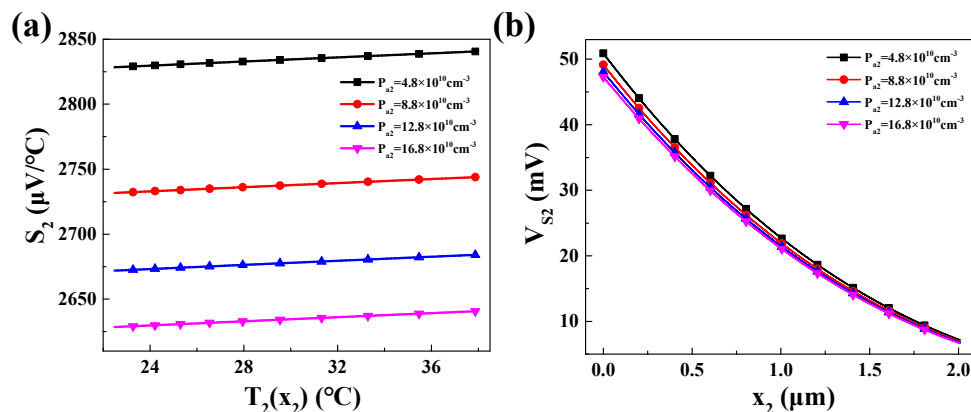


Figure 11. Under different doping concentrations  $P_{a2}$ : (a) the relationship between Seebeck coefficient  $S_2$  and temperature; (b) variation in Seebeck voltage  $V_{S2}$  at different  $x_2$  positions.

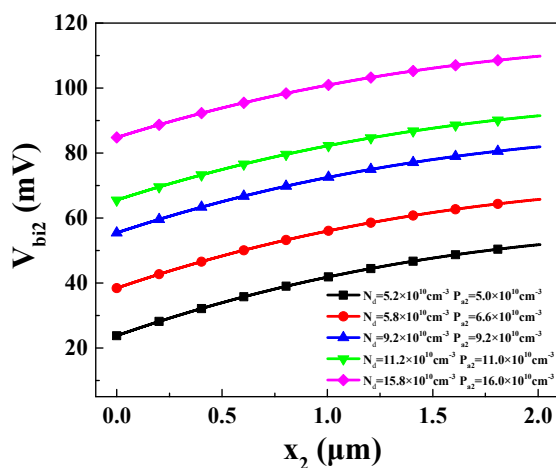


Figure 12. Different values of built-in voltage in P<sub>2</sub>-N region on different  $x_2$ .

Based on Section 2.3.2, it can be concluded that achieving the forward bias and forward conduction of the emitter–base junction depends on three conditions:  $V_{bi2}(x_2) > 0$  and  $p_2(x_2) < N_d$ . These conditions are all influenced by  $P_{a2}$ ,  $x_2$ , and  $N_d$ . Therefore, the reverse bias in the base–collector junction can be achieved by adjusting the concentrations of  $P_{a2}$  and  $N_d$ . The appropriate concentration ranges for  $P_{a2}$  and  $N_d$  are shown in Figure 13.

Unlike the previous section, the range of  $N_d$  is from  $5.2 \times 10^{10} \text{ cm}^{-3}$  to  $15.8 \times 10^{10} \text{ cm}^{-3}$ . It can be observed that, as  $N_d$  increases, the corresponding range of  $P_{a2}$  also gradually increases. This is because higher values of  $N_d$  and  $P_{a2}$  both lead to larger values of  $V_{bi2}(x_2)$ , making it easier to satisfy the reverse biasing condition  $V_{bi2}(x_2) > 0$ .

To summarize, when  $N_d$  is within the range of  $5.2 \times 10^{10} \text{ cm}^{-3}$  to  $15.8 \times 10^{10} \text{ cm}^{-3}$ , the thermoelectric transistor can be activated in the forward-active mode. The corresponding ranges of  $P_{a1}$ ,  $P_{a2}$ ,  $x_1$ , and  $x_2$  are determined by the different values of  $N_d$ . By adjusting the concentrations of  $P_{a1}$ ,  $N_d$ , and  $P_{a2}$ , the current can be generated in the thermoelectric transistor directly driven by the Seebeck effect.

### 3.4. Output Performance of Thermoelectric Transistor

It is evident that the output power of the transistor is primarily influenced by  $P_{a1}$ ,  $N_d$ ,  $P_{a2}$ ,  $x_1$ , and  $x_2$  based on Equation (44). Therefore, the impact of these parameters on the output power of the thermoelectric transistor is obtained in the following.

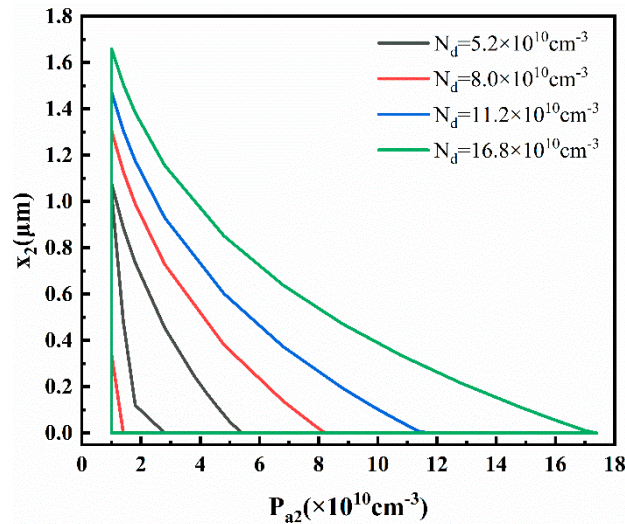


**Figure 13.** Suitable range and corresponding  $x_2$  value of  $P_{a2}$  that satisfies forward bias and forward conduction of emitter–base.

#### 3.4.1. Impact of $N_d$ on Output Power of Thermoelectric Transistor

Since the value of  $N_d$  directly affects the other four physical quantities, it is essential to initially examine the influence of  $N_d$  on the output power. Figure 14 illustrates the relationship between  $N_d$  and the maximum output power of the thermoelectric transistor.

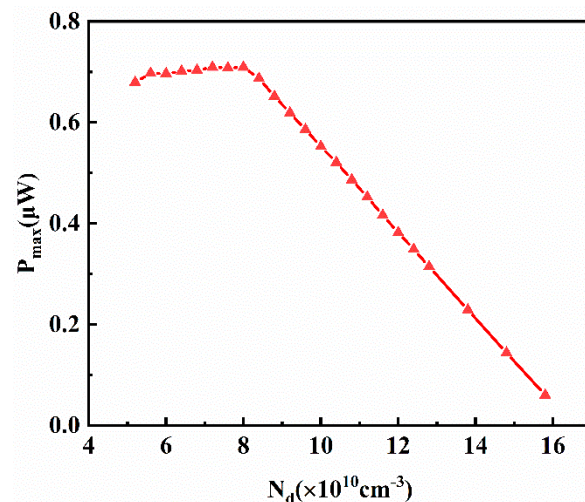


**Figure 14.** Variation in the maximum output power  $P_{max}$  of the transistor with the value of  $N_d$ .

It is evident that, as  $N_d$  gradually increases,  $P_{outmax}$  exhibits a trend of initially increasing and then decreasing. At  $N_d = 8.0 \times 10^{10} \text{ cm}^{-3}$ ,  $P_{outmax}$  reaches its maximum value of  $0.7093 \mu\text{W}$ . It is important to note that different values of  $N_d$  correspond to various combinations of  $P_{a1}$ ,  $P_{a2}$ ,  $x_1$ , and  $x_2$ . Considering the multitude of possible parameter combinations, it is challenging to directly explain how  $N_d$  influences the output power. Therefore, a comprehensive enumeration of the parameters is necessary to identify the optimal solution, which, in this case, is  $N_d = 8.0 \times 10^{10} \text{ cm}^{-3}$  and  $P_{outmax} = 0.7093 \mu\text{W}$ .

### 3.4.2. Impact of $P_{a1}$ and $x_1$ on Output Power of Thermoelectric Transistor

For  $N_d = 8.0 \times 10^{10} \text{ cm}^{-3}$ , the range of  $P_{a1}$  is from  $1.61 \times 10^{18} \text{ cm}^{-3}$  to  $2.6 \times 10^{18} \text{ cm}^{-3}$  and the range of  $P_{a2}$  is from  $1.0 \times 10^{10} \text{ cm}^{-3}$  to  $8.2 \times 10^{10} \text{ cm}^{-3}$ . Moreover, different values of  $P_{a1}$  and  $P_{a2}$  correspond to specific ranges of  $x_1$  and  $x_2$ . Considering a fixed  $P_{a2}$  value of  $7.8 \times 10^{10} \text{ cm}^{-3}$  and  $x_2$  value of  $0.4 \text{ }\mu\text{m}$ , the relationship between output power ( $P_{out}$ ) and the variations in  $P_{a1}$  and  $x_1$  is illustrated in Figure 15.

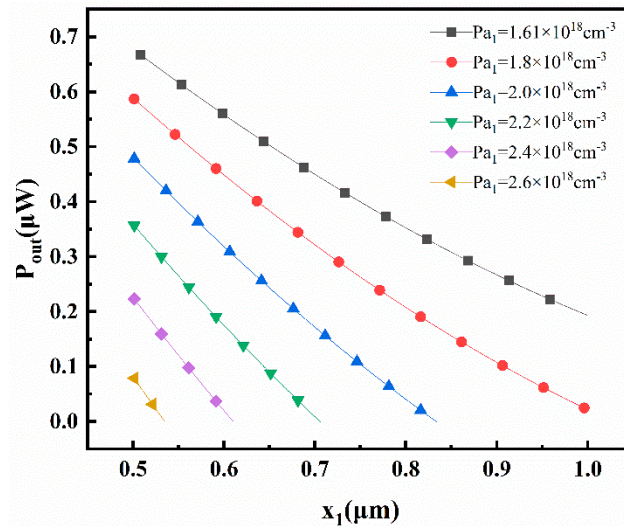


Figure 15. Variation in the maximum output power of transistor  $P_{out}$  with the values of  $P_{a1}$  and  $x_1$ .

It can be observed that the output power ( $P_{out}$ ) increases as the concentration of  $P_{a1}$  and  $x_1$  decrease. These results can be derived from Equation (58):

$$P_{out} = I_e(x_1) \times [V_{bi2}(x_2) - V_{s2}(x_2)] \tag{58}$$

When  $N_d$ ,  $P_{a2}$ , and  $x_2$  remain constant, the value of  $P_{out}$  is primarily influenced by  $I_e(x_1)$ :

$$I_e(x_1) = \frac{V_{s1}(x_1) - V_{bi1}(x_1)}{R_e(x_1)} \tag{59}$$

At  $x_1 = 1 \text{ }\mu\text{m}$ , both  $V_{bi1}(x_1)$  and  $V_{s1}(x_1)$  reach their maximum values. However, compared to  $V_{s1}(x_1)$ ,  $V_{bi1}(x_1)$  increases more rapidly as  $x_1$  increases. Therefore, at  $x_1 = 0.501 \text{ }\mu\text{m}$ ,  $V_{s1}(x_1) - V_{bi1}(x_1)$  reaches its maximum value. Thus, as  $x_1$  decreases within the range of  $x_1 \in (0.501 \text{ }\mu\text{m}, 1 \text{ }\mu\text{m})$ ,  $P_{out}$  increases. On the other hand, when other conditions remain unchanged, a larger  $P_{a1}$  leads to a higher built-in voltage in the  $P_1$  region ( $V_{s1}(x_1) - V_{bi1}(x_1)$ ). As a result, with an increase in  $P_{a1}$ ,  $P_{out}$  decreases.

### 3.4.3. Impact of $P_{a2}$ and $x_2$ on Output Power of Thermoelectric Transistor

The impact of  $P_{a2}$  and  $x_2$  on the output power of the thermoelectric transistor is examined in the following when  $P_{a1} = 1.61 \times 10^{18} \text{ cm}^{-3}$  and  $x_1 = 0.508 \text{ }\mu\text{m}$ . As shown in Figure 16, it can be observed that  $P_{out}$  increases as  $P_{a2}$  increases and  $x_2$  decreases. Again, referring to the expression for  $P_{out}$ :

$$P_{out} = I_e(x_1) \times [V_{bi2}(x_2) - V_{s2}(x_2)] \tag{60}$$

When  $N_d$ ,  $P_{a1}$ , and  $x_1$  are constant, the value of  $P_{out}$  is mainly influenced by  $V_{bi2}(x_2) - V_{s2}(x_2)$ . An increase in  $P_{a2}$  leads to a higher value of  $V_{bi2}(x_2)$ , resulting in a larger difference between  $V_{bi2}(x_2)$  and  $V_{s2}(x_2)$ . Consequently, as  $P_{a2}$  increases,  $P_{out}$  also increases. On the other hand, when  $x_2$  increases,  $\Delta T_2(x_2)$  decreases, resulting in a lower  $V_{s2}(x_2)$  and higher  $V_{bi2}(x_2)$ . In

this case,  $V_{s2}(x_2)$  dominates the relationship and the value of  $V_{bi2}(x_2) - V_{s2}(x_2)$  decreases, leading to a decrease in  $P_{out}$ .

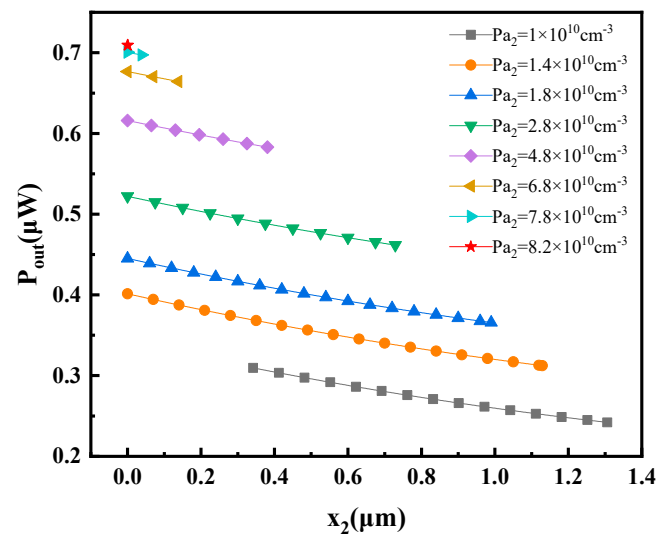


**Figure 16.** Variation in the maximum output power of transistor  $P_{out}$  with the values of  $P_{a2}$  and  $x_2$ .

#### 3.4.4. Transistor Structure: Optimization of Output Power Effects

As deduced from the above analysis, when  $N_d = 8.0 \times 10^{10} \text{ cm}^{-3}$ ,  $P_{a1} = 1.61 \times 10^{18} \text{ cm}^{-3}$ ,  $P_{a2} = 8.2 \times 10^{10} \text{ cm}^{-3}$ ,  $x_1 = 0.508 \text{ }\mu\text{m}$ , and  $x_2 = 0 \text{ }\mu\text{m}$ , the maximum output power of this designed thermoelectric transistor can reach  $0.7093 \text{ }\mu\text{W}$ .

If only  $\text{Bi}_2\text{Te}_3$  is used without the thermoelectric transistor structure, the output power, can be calculated as  $0.1442 \text{ }\mu\text{W}$ . It can be observed that the designed thermoelectric transistor structure in this work results in an increase in the output power compared to a single thermoelectric material, with an improvement of 391.9%.

## 4. Conclusions

In this work, the temperature distribution and hole concentration distribution within the thermoelectric transistor is obtained through theoretical calculations. By considering the variation in the built-in voltage with temperature, the formation principle of the thermoelectric transistor is demonstrated. Subsequently, based on the operation conditions of the thermoelectric transistor, suitable doping concentrations of the emitter, base, and collector can be determined. Furthermore, the maximum output power of the thermoelectric transistor is obtained. The main conclusions drawn from this work are as follows:

- (i) The thermoelectric transistor, composed of  $\text{P}_1\text{-Bi}_2\text{Te}_3$ ,  $\text{N-Si}$ , and  $\text{P}_2\text{-Si}$ , is directly irradiated by the laser. Under laser illumination and heat conduction, the temperature decreases from  $66.7 \text{ }^\circ\text{C}$  to  $20 \text{ }^\circ\text{C}$ , creating a temperature difference of  $46.7 \text{ }^\circ\text{C}$  at the two ends of the thermoelectric transistor. As a result of the temperature difference, holes inside  $\text{P}_1$  and  $\text{P}_2$  regions migrate from the hot end to the far end, leading to increased hole concentration at the cold end.
- (ii) The operation conditions of the thermoelectric transistor under laser irradiation are investigated. Based on the corresponding conditions, suitable doping concentrations of the emitter, base, and collector can be determined. By adjusting these concentrations, the current can be produced in the thermoelectric transistor only driven by the Seebeck effect.
- (iii) The influence of these parameters on the output power of the thermoelectric transistor is also investigated. The maximum output power of the thermoelectric transistor is  $0.7093 \text{ }\mu\text{W}$  under a temperature difference of  $46.7 \text{ }^\circ\text{C}$ , which is nearly quadrupling the performance compared to the single thermoelectric material structure.

- (iv) Importantly, the operation conditions of the thermoelectric transistor established in this work are applicable to other material systems. By adjusting the doping concentration within each region, current can be generated, ensuring that the forward-active mode is achieved. Therefore, this novel thermoelectric generator concept can significantly contribute to the advancement of the thermoelectric field. Moreover, the combination with transistor technology can expand the range of applications for thermoelectric generators.

**Author Contributions:** H.D.: conceptualization, methodology, formal analysis, writing—original draft; B.N.: conceptualization, methodology, formal analysis, writing—original draft; G.X.: investigation, supervision, conceptualization, principle proposal, funding acquisition. All authors have read and agreed to the published version of the manuscript.

**Funding:** This work was financially supported by The National Key Research and Development Program of China (Grant No. 2017YFF0204706), by The Fundamental Research Funds for the Central Universities (Grant No. FRF-MP-18-005, and FRFMP-19-005).

**Institutional Review Board Statement:** Not applicable.

**Informed Consent Statement:** Not applicable.

**Data Availability Statement:** The data presented in this study are available upon request from the corresponding author.

**Conflicts of Interest:** The authors declare no conflict of interest.

## References

1. Graus, W.H.J.; Voogt, M.; Worrell, E. International comparison of energy efficiency of fossil power generation. *Energy Policy* **2007**, *35*, 3936–3951. [[CrossRef](#)]
2. Mallick, M.; Franke, L.; Rösch, A.G.; Geßwein, H.; Long, Z.; Eggeler, Y.M.; Lemmer, U. High Figure-of-Merit Telluride-Based Flexible Thermoelectric Films through Interfacial Modification via Millisecond Photonic-Curing for Fully Printed Thermoelectric Generators. *Adv. Sci.* **2022**, *9*, 2202411. [[CrossRef](#)] [[PubMed](#)]
3. Shittu, S.; Li, G.-Q.; Zhao, X.-D.; Ma, X.-L. Review of thermoelectric geometry and structure optimization for performance enhancement. *Appl. Energy* **2020**, *268*, 115075. [[CrossRef](#)]
4. Yang, F.; Wu, J.; Suwardi, A.; Zhao, Y.-S.; Laing, B.-Y.; Jiang, J.; Xu, J.-W.; Chi, D.-Z.; Hippalgaonkar, K.; Lu, J.-P.; et al. Gate-Tunable Polar Optical Phonon to Piezoelectric Scattering in Few-Layer Bi<sub>2</sub>O<sub>2</sub>Se for High-Performance Thermoelectrics. *Adv. Mater.* **2021**, *4*, 33.
5. Wu, X.-M.; Gao, G.-Y.; Hu, L.; Qin, D. 2D Nb<sub>2</sub>SiTe<sub>4</sub> and Nb<sub>2</sub>GeTe<sub>4</sub>: Promising thermoelectric figure of merit and gate-tunable thermoelectric performance. *Nanotechnology* **2021**, *32*, 245203. [[CrossRef](#)] [[PubMed](#)]
6. Bejenari, I.; Kantser, V.; Balandin, A.A. Thermoelectric properties of electrically gated bismuth telluride nanowires. *Phys. Rev. B.* **2010**, *81*, 075316. [[CrossRef](#)]
7. Qin, D.-L.; Pan, F.; Zhou, J.; Xu, Z.-B.; Deng, Y. High ZT and performance controllable thermoelectric devices based on electrically gated bismuth telluride thin films. *Nano Energy* **2021**, *89*, 106472. [[CrossRef](#)]
8. Nan, B.; Xu, G.; Liu, W.-M.; Yang, Q.; Zhang, B.; Dong, Y.; Tie, J.; Guo, T.; Zhou, X. High thermoelectric performance of PNP abrupt heterostructures by independent regulation of the electrical conductivity and Seebeck coefficient. *Mater. Today Commun.* **2022**, *31*, 103343. [[CrossRef](#)]
9. Nan, B.; Xu, G.; Yang, Q.; Zhang, B.; Zhou, X. Innovative design and optimized performance of thermoelectric transistor driven by the Seebeck effect. *Energ. Convers. Manag.* **2023**, *283*, 116880. [[CrossRef](#)]
10. Hua, Z.J.; Zhang, X.; Tu, D.-W.; Wang, X.-Z.; Haung, N.-D. Learning to high-performance autofocus microscopy with laser illumination. *Measurement* **2023**, *216*, 112964. [[CrossRef](#)]
11. Shi, Q.; Li, J.; Zhao, X.-W.; Chen, Y.-Y.; Zhang, F.-J.; Zhong, Y.; Ang, R. Comprehensive Insight into p-Type Bi<sub>2</sub>Te<sub>3</sub>-Based Thermoelectrics near Room Temperature. *ACS Appl. Mater. Interfaces* **2022**, *14*, 49425–49445. [[CrossRef](#)]
12. Dashevsky, Z.; Skipidarov, S. Investigating the performance of bismuth-antimony telluride. In *Novel Thermoelectric Materials and Device Design Concepts*; Springer: Berlin/Heidelberg, Germany, 2019; pp. 3–21.
13. Maksymuk, M.; Dzunza, B.; Matkivsky, O.; Horichok, I.; Shneck, R.; Dashevsky, Z. Development of the high performance thermoelectric uncouple based on Bi<sub>2</sub>Te<sub>3</sub> compounds. *J. Power Sources* **2022**, *530*, 231301. [[CrossRef](#)]
14. Li, L.-B.; Xu, H.-W.; Yang, H.-B.; Huang, S.-L.; Yang, H.; Li, Y.-A.; Zhang, Q.; Guo, Z.; Hu, H.-Y.; Sun, P.; et al. Design of Bi<sub>2</sub>Te<sub>3</sub>-based thermoelectric generator in a widely applicable system. *J. Power Sources* **2023**, *559*, 232661.
15. Maksymuk, M.; Parashchuk, T.; Dzunza, B.; Nvkvrui, L.; Chernyak, L.; Dashevsky, Z. Highly efficient bismuth telluride-based thermoelectric microconverters. *Mater. Today Energy* **2021**, *21*, 100753. [[CrossRef](#)]

16. Zhu, B.; Liu, X.-X.; Wang, Q.; Qiu, Y.; Shu, Z.; Guo, Z.-T.; Tong, Y.; Cui, J.; Gu, M.; He, J.-Q. Realizing record high performance in n-type Bi<sub>2</sub>Te<sub>3</sub>-based thermoelectric materials. *Energy Environ. Sci.* **2020**, *13*, 2106–2114. [[CrossRef](#)]
17. Costa, L.D.F.; Silva, F.N.; Comin, C.H. Characterizing BJTs using the Early voltage in the forward active mode. *Int. J. Circuit Theory App.* **2018**, *46*, 978–986. [[CrossRef](#)]
18. Bhattacharya, D.; Singh, R.; Holloway, P. Laser-target interactions during pulsed laser deposition of superconducting thin films. *J. Appl. Phys.* **1991**, *70*, 5433–5439. [[CrossRef](#)]
19. Ge, Y.; He, K.; Xiao, L.-H.; Yuan, W.-Z.; Huang, S.-M. Geometric optimization for the thermoelectric generator with variable cross-section legs by coupling finite element method and optimization algorithm. *Renew. Energy* **2022**, *183*, 294–303. [[CrossRef](#)]
20. Fu, D.; Levander, A.-X.; Zhang, R.; Ager, J.-W., III; Wu, J. Electrothermally driven current vortices in inhomogeneous bipolar semiconductors. *Phys. Rev. B.* **2011**, *84*, 045205. [[CrossRef](#)]
21. Ravich, Y.I.; Pshenai-Severin, D. Thermoelectric figure of merit of a pn junction. *Semiconductors* **2001**, *35*, 1161–1165. [[CrossRef](#)]
22. Lv, T.; Li, Z.-M.; Yang, Q.-X.; Benton, A.; Zheng, H.-T.; Xu, G.-Y. Synergistic regulation of electrical-thermal effect leading to an optimized thermoelectric performance in Co doping n-type Bi<sub>2</sub>(Te<sub>0.97</sub>Se<sub>0.03</sub>)<sub>3</sub>. *Intermetallics* **2020**, *118*, 106683. [[CrossRef](#)]
23. Snyder, G.-J.; Toberer, E.-S. Complex thermoelectric materials. *Nat. Mater.* **2008**, *7*, 105–114. [[CrossRef](#)]
24. Chavez, R.; Angst, S.; Hall, J.; Stoetzel, J.; Kessler, V.; Bitzer, L.; Maculewicz, F.; Benson, N.; Wiggers, H.; Wolf, D.; et al. Temperature Thermoelectric Device Concept Using Large Area PN Junctions. *J. Electron. Mater.* **2014**, *43*, 2376. [[CrossRef](#)]
25. Neamen, D.-A. *Microelectronics: Circuit Analysis and Design*, 3rd ed.; McGraw-Hill: New York, NY, USA, 2007.
26. Ahmad, F.; Singh, R.; Misra, P.-K.; Kumar, N.; Kumar, R.; Kumar, P. Fabrication of a p-n heterojunction using topological insulator Bi<sub>2</sub>Te<sub>3</sub>-Si and its annealing response. *J. Electron Mater.* **2018**, *47*, 6972–6983. [[CrossRef](#)]
27. Zhou, J.; Li, X.-B.; Chen, G.; Yang, R.-G. Semiclassical model for thermoelectric transport in nanocomposites. *Phys. Rev. B.* **2010**, *82*, 115308. [[CrossRef](#)]
28. Xu, G.-Y.; Ren, P.; Lin, T.; Wu, X.-F.; Zhang, Y.-H.; Niu, S.-T.; Bailey, T.P. Mechanism and application method to analyze the carrier scattering factor by electrical conductivity ratio based on thermoelectric property measurement. *J. Appl. Phys.* **2018**, *123*, 015101. [[CrossRef](#)]
29. Chen, X.; Wang, Y.-C.; Ma, Y.-M.; Cui, T.; Zou, G.-T. Origin of the High Thermoelectric Performance in Si Nanowires: A First-Principle Study. *J. Phys. Chem. C.* **2009**, *113*, 14001–14005. [[CrossRef](#)]
30. Yamasaka, S.; Watanabe, K.; Sakane, S.; Takeuch, S.; Sakai, A.; Sawano, K.; Nakamura, Y. Independent control of electrical and heat conduction by nanostructure designing for Si-based thermoelectric materials. *Sci. Rep.* **2016**, *6*, 22838. [[CrossRef](#)]

**Disclaimer/Publisher’s Note:** The statements, opinions and data contained in all publications are solely those of the individual author(s) and contributor(s) and not of MDPI and/or the editor(s). MDPI and/or the editor(s) disclaim responsibility for any injury to people or property resulting from any ideas, methods, instructions or products referred to in the content.